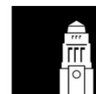

This is a repository copy of *Optimization of photomixers and antennas for continuous-wave terahertz emission*.

White Rose Research Online URL for this paper:
http://eprints.whiterose.ac.uk/732/

Article:

Gregory, I.S., Baker, C., Tribe, W.R. et al. (5 more authors) (2005) Optimization of photomixers and antennas for continuous-wave terahertz emission. IEEE Journal of Quantum Electronics, 41 (5). pp. 717-728. ISSN 0018-9197

https://doi.org/10.1109/JQE.2005.844471

Reuse
See Attached

Takedown
If you consider content in White Rose Research Online to be in breach of UK law, please notify us by emailing eprints@whiterose.ac.uk including the URL of the record and the reason for the withdrawal request.

eprints@whiterose.ac.uk
https://eprints.whiterose.ac.uk/

Optimization of Photomixers and Antennas for Continuous-Wave Terahertz Emission

Ian S. Gregory, Colin Baker, William R. Tribe, Ian V. Bradley, Michael J. Evans, Edmund H. Linfield, A. Giles Davies, and Mohamed Missous, *Member, IEEE*

***Abstract*—We have studied terahertz emission from interdigitated finger photomixers coupled to planar antenna structures. Using both pulsed and continuous-wave excitation, polarization measurements reveal that the antenna design dominates the properties of the radiated output at frequencies below 0.6 THz, while the efficiency at higher frequencies is additionally dependent on the design of the photomixer fingers. We have produced terahertz maps of the device, characterizing the photomixer by measuring the generated power as a function of the excitation position. Together, these measurements have allowed us to understand better the distinct roles of the photomixer and antenna in emission at different frequencies and, hence, independently optimize these components.**

***Index Terms*—Continuous-wave (CW), LT-GaAs, photoconductive antenna, photomixer, terahertz.**

I. Introduction

The terahertz region of the electromagnetic spectrum ranges from 100 GHz to 10 THz, between the millimeter and the far-infrared frequencies. Compared to many other regions of the spectrum, scientific and technological progress at terahertz frequencies has been largely impeded by a lack of coherent sources and detectors. Although such devices are commonplace at the infrared and microwave extremes of the terahertz range, they cannot be easily modified to work at terahertz frequencies. Recent developments have started to address this issue, and a variety of novel emitters and detectors based on semiconductor technology are emerging [1]–[4]. Terahertz radiation is nonionizing, has a shorter wavelength, and hence higher resolution, than microwaves, and is minimally attenuated by many common materials. Consequently, the technological advances have been accompanied by much interest in possible applications in fields including security screening [5], spectroscopy, and medical imaging [6].

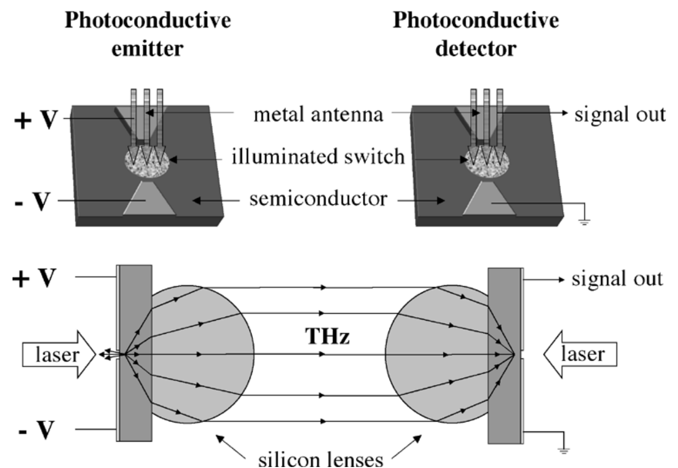

Fig. 1. Schematic diagram of the photoconductive emitter and identical detector, showing the metallic planar antennas, illuminated photoconductive switches, and the silicon lenses. The same arrangement is employed for both pulsed and CW-THz implementations.

Established experimental terahertz systems are largely based on photoconductive switches, which rely on the production of few-cycle terahertz pulses using an ultrafast (femtosecond) laser to excite a photoconductive antenna. This technique is inherently broadband, with the emitted power distributed over several terahertz. In the emitter, a transient change in the resistance of a photoconductive switch occurs on a terahertz timescale when illuminated by a laser pulse. Application of an external dc bias across the switch creates a current flow that contains components at terahertz frequencies. These currents induce a terahertz electromagnetic field in the planar, metallic antenna connected to the switch. The resulting terahertz dipole radiation is coupled from the antenna into free space as a quasi-collimated beam using a high-resistivity hyper-hemispherical silicon lens [7]. Optoelectronic detection is possible by measuring the current induced in a similar antenna circuit by the incoming terahertz radiation [8]–[11]. By gating the receiver switch with a second femtosecond pulse synchronized to the terahertz emission, a dc signal may be measured. Varying the optical path length to the receiver allows the entire terahertz time domain to be sampled. Hence both the amplitude and phase of the incident terahertz wave can be obtained, and a dynamic range of 60 dB demonstrated using time-gated detection [12]. Fig. 1 shows a schematic diagram of the photoconductive switch and antenna,

Manuscript received July 19, 2004; revised September 21, 2004. This work was supported in part by an EC-Framework V program (WANTED), the EPSRC, the Royal Society (A. G. Davies) and in part by Toshiba Research Europe Ltd. (E. H. Linfield). Aspects of this work are contained in U.K. Patent Application 0221056.5.

I. S. Gregory is with the Semiconductor Physics Group, Cavendish Laboratory, University of Cambridge, Cambridge CB3 0HE, U.K., and also with TeraView Ltd., Cambridge CB4 0WS, U.K. (e-mail: ian.gregory@teraview.com).

C. Baker, W. R. Tribe, I. V. Bradley, and M. J. Evans are with TeraView Ltd., Cambridge CB4 0WG, U.K. (e-mail: colin.baker@teraview.com; bill.tribe@teraview.com; ian.bradley@teraview.com; michael.evans@teraview.com).

E. H. Linfield and A. G. Davies are with the School of Electronic and Electrical Engineering, University of Leeds, Leeds LS2 9JT, U.K. (e-mail: e.h.linfield@leeds.ac.uk; g.davies@leeds.ac.uk).

M. Missous is with the Department of Electrical Engineering and Electronics, University of Manchester Institute of Science and Technology, Manchester M60 1QD, U.K. (e-mail: missous@umist.ac.uk).

Digital Object Identifier 10.1109/JQE.2005.844471

0018-9197/$20.00 © 2005 IEEE

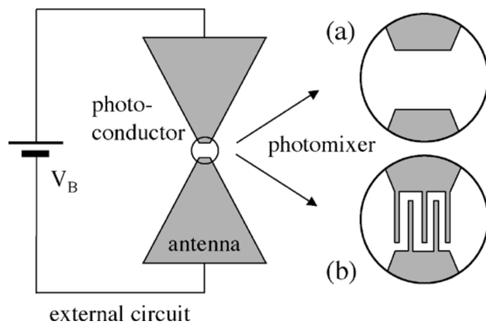

Fig. 2. Schematic diagram of a CW-THz device, consisting of an antenna coupled to the external circuit. Inset are two designs for electrodes: (a) simple photoconductive gap and (b) with interdigitated fingers attached. The structure shown in the inset, comprising the photoconductor and electrodes, is generally termed the "photomixer."

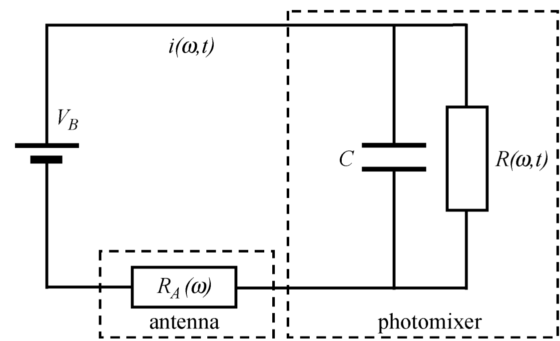

Fig. 3. Equivalent circuit diagram for the photomixer and antenna. Current drawn from the bias source is modulated at angular frequency ω by the photoconductor, with resistance $R(\omega, t)$. The capacitance C represents the effects of the charge accumulating at the electrodes. Power is dissipated in the antenna, $R_A(\omega)$, of which the component oscillating with angular frequency ω is coupled out as terahertz radiation.

along with a typical free-space terahertz system incorporating silicon lenses.

Terahertz-pulsed imaging has been widely reported [6], [13], [14], with image capture by serial pixel collection. Since information about the entire waveform is available at each pixel, a spectroscopic analysis is simultaneously possible. However, the commercial application of such systems has highlighted a number of limitations. Primarily, the femtosecond laser and associated chillers and power supplies are bulky and expensive, and thus not ideal for portable terahertz systems for use outside of the research laboratory.

An alternative approach to terahertz systems is optical heterodyne conversion, or photomixing, which can be achieved using two continuous-wave (CW) lasers [15], [16]. The mixing of two above-bandgap (visible or near-infrared) wavelengths produces beating, which can modulate the conductance of a photoconductive switch (semiconductor) at the terahertz difference frequency. Upon application of a bias, monochromatic CW-terahertz (CW-THz) radiation is produced. Furthermore, Verghese *et al.* have demonstrated that coherent homodyne detection is possible in the reverse scheme [17], in analogy with the optical gating mechanism for photoconductive detection of pulsed terahertz radiation. Since these all-photoconductive systems can be driven by inexpensive, compact and tunable diode lasers [18], [19] they may become a cost-effective commercial terahertz product.

The design of CW-THz emitters and detectors consists of several distinct components. These are the photoconductor, specifically the semiconductor material, the electrodes, which define the geometrical arrangement of the photoconductive gap, and the antenna. A schematic of a typical CW-THz device is shown in Fig. 2. The performance of such a device can be understood and optimized by considering separately the roles of the various components, and applying an equivalent electrical circuit model to analyze their interconnection. The role of the photoconductor is to provide a modulated conductivity in response to the optical field, through the photo-creation of electron–hole pairs. The electrodes couple the charge within the photoconductor to the antenna and external circuit, and their design is used to optimize the efficiency of the optical modulation. The antenna is designed to optimize the coupling between the circuit and free-space electromagnetic radiation modes.

The antenna and electrodes are, of course, a connected metallic structure, and are bonded to the external circuit. For emitters, this allows a bias to be applied to the photoconductive gap (as shown in Fig. 2), or for receivers the current flow can be measured. The electrodes and photoconductive gap are generically termed the photomixer; the element responsible for modulating the response of the electrical circuit according to the optical field. The equivalent circuit for the photomixer, antenna and external circuit is shown in Fig. 3.

While the simple modulation of conductance mechanism may be clear, the role of the antenna in coupling charge movement to free-space radiation is less so. Dipole separation and terahertz emission can occur in the absence of an antenna and an applied bias, as in the observation of surface field terahertz emission [20]. The emitted power can, however, be increased by using electrodes to apply an external bias that exceeds that associated with the surface depletion field. Nevertheless, even in this case, radiation to free space may still arise from charge movement within the photoconductor itself, prior to charge transfer to the electrodes of the circuit, and radiation from a coupled antenna.

An additional enhancing effect of adding the semiconductor-metal junction may be inferred from the increased terahertz power observed when carriers are optically injected near to the anode [21]. This "near-anode" enhancement is explained by the highly nonlinear electric field distribution across the photoconductive gap, caused by the formation of a space charge field at the interface. A similar enhancement is seen when near singular electric fields are produced using a sharp "bow-tie" geometry for the electrodes [22]. This is attributed to an enhanced contribution from the fields associated with the flux of excited carriers that reach the interfaces before scattering, and is particularly prominent at the anode, since the mobility of the electrons is greater than that of the holes.

The motivation for the work presented here is the systematic optimization of photomixer and antenna structures for all-optoelectronic CW-THz imaging systems [19], [23], [24], using all of the design criteria discussed above. The theory of photomixing, and the equations governing the power transformed to terahertz radiation are presented in Section II, to allow the parameters governing the overall device performance to be determined. Sections III–V then summarize and address the re-

quirements imposed upon the photoconductor material, electrodes and antenna design, respectively. The electrode design is assessed using terahertz maps to deduce the contribution to the terahertz emission from illumination of different parts of the photomixer structure. These maps are used to determine the optimum electrode geometry, using the near-anode enhancement to improve the efficiency of modulation from the photomixer. Section V details design considerations for the antenna, with numerical simulations to calculate the frequency response. Section VI then describes our experimental work to correlate the terahertz polarization with the frequency of emission, allowing inferences to be made regarding the separate role of the photoconductor and antenna in emission at different frequencies.

II. Photomixing Mechanism

For two visible or near-infrared CW laser beams, collinear in space and with aligned linear polarization, the total electric field is the linear sum of the two individual fields, modulated at the difference frequency. Owing to the finite excitation and decay times for the photo-created carriers, a semiconductor is able to respond only to the slower difference frequency beats, allowing an oscillation in the conductance to be produced at terahertz frequencies. Thus terms that vary at optical frequencies, ν_1, ν_2 or $\nu_1+\nu_2$, may be replaced by their mean (time-averaged) values. For two beams with powers P_1 and P_2, and frequencies ν_1 and ν_2, the combined instantaneous power incident upon the semiconductor is then

$$P(\omega,t)=P_1+P_2+2\sqrt{mP_1P_2}\cos(\omega t) \tag{1}$$

where $\omega=2\pi(\nu_1-\nu_2)$, and m is introduced as a parameter to describe the quality of the spatial overlap, and varies between 0 (no overlap) and 1 (perfectly matched) [15].

The carrier density in the photoconductive gap may be described by

$$\frac{dn}{dt}=\frac{\eta}{h\nu Ad}P(\omega,t)-\frac{n}{\tau} \tag{2}$$

where n is the instantaneous number density of electron–hole pairs, η is the external quantum efficiency (number of photocreated carrier pairs per incident photon), A is the active area (presumed equal to the laser spot area), and d is the absorption depth. $h\nu$ is the mean photon energy of the visible/near-infrared laser beam. The second term in (2) gives the exponential decay of carriers from the conduction band with a $1/e$ decay lifetime characterized by τ. Substituting (1) into (2) gives a differential equation with the analytical solution

$$n(\omega,t)=\frac{\eta(P_1+P_2)\tau}{h\nu Ad}\left[1+\frac{2\sqrt{mP_1P_2}}{P_1+P_2}\right]\times\left[\frac{\omega\tau\sin(\omega t)+\cos(\omega t)}{1+(\omega\tau)^2}\right]. \tag{3}$$

Factors of the form $1-Ce^{-t/\tau}$ also appear, but are neglected since they saturate on picosecond timescales. Ignoring the resistance of the contacts, the time-dependent conductance, $G(\omega,t)$ of the photoconductive gap may be written as

$$G(\omega,t)\approx\frac{\sigma d\sqrt{A}}{r}=\frac{\mu ed\sqrt{A}}{r}n(\omega,t) \tag{4}$$

where σ is the bulk conductivity, μ is the effective carrier mobility, and r is the width of the photoconductive gap. Thus together, (3) and (4) give an estimate of the time-dependent conductance of the photoconductive gap.

Using the equivalent electrical circuit shown in (Fig. 3), the total impedance is given by

$$Z(\omega,t)=R_A+[G(\omega,t)+j\omega C]^{-1}. \tag{5}$$

When a dc bias of V_B is applied to the external circuit, the instantaneous power dissipated in the load (antenna) resistance is

$$P_{\text{antenna}}(\omega,t)=R_A\left[\frac{V_B}{Z(\omega,t)}\right]^2. \tag{6}$$

Substituting (3)–(5) into (6), taking the real part, and using the fact that $R_AG\ll 1$, gives a closed form expression for the total instantaneous power dissipated in the antenna. This contains both terahertz (ac) and Joule heating (dc) components

$$P_{\text{antenna}}(\omega,t)=\frac{R_AV_B^2}{A}\left[\frac{\eta\mu e\tau}{rh\nu}\right]^2\frac{1}{1+(\omega R_AC)^2}\times\left[P_1+P_2+\frac{2\sqrt{mP_1P_2}}{1+(\omega\tau)^2}(\omega\tau\sin(\omega t)+\cos(\omega t))\right]^2. \tag{7}$$

The mean power of the terahertz component may be found by disregarding the constant offset and averaging the sinusoidal terms, to give an expression consistent with that derived by Brown *et al.* [15]

$$P_{\text{THz}}(\omega)=2\frac{R_AV_B^2}{A}\left[\frac{\eta\mu e\tau}{rh\nu}\right]^2\frac{mP_1P_2}{[1+(\omega\tau)^2][1+(\omega R_AC)^2]}. \tag{8}$$

The Joule heating may be found by solving (2) for the steady state solution (using a constant, time averaged value of P). Thus the energy dissipated in the photoconductor resistance is given by

$$P_{\text{Joule}}(\omega)=\bar{G}V_B^2=\frac{\eta\mu e\tau}{rh\nu}\frac{V_B^2}{\sqrt{A}}(P_1+P_2). \tag{9}$$

In practice, the applied bias is governed by the current threshold at which the power dissipated as heat in (9) causes damage to the device. Thus, back substituting from (9) for the bias in (8) gives the maximum emitted terahertz power at the dc power limit for the photoconductor. This is equivalent to running the device at a constant dc current compliance

$$P_{\text{THz}}^{\max}(\omega)=2\frac{R_AP_{\text{Joule}}}{\sqrt{A}}\left[\frac{\eta\mu e}{rh\nu}\right]\left[\frac{mP_1P_2}{P_1+P_2}\right]\times\frac{\tau}{[1+(\omega\tau)^2][1+(\omega R_AC)^2]}. \tag{10}$$

Equation (10) has the following properties. The output power available is maximized for $m=1$ (perfect overlap), and $P_1=P_2$, when the total incident laser power is kept constant. At high frequency, $P_{\text{THz}}(\omega)\sim\omega^{-4}$, and thus a roll-off of 12 dB per octave is expected. Differentiation of (10) with respect to τ yields the condition for the optimum carrier lifetime in the material

$$\omega\tau_{\text{opt}}=2\pi\nu_{\text{THz}}\tau_{\text{opt}}=1. \tag{11}$$

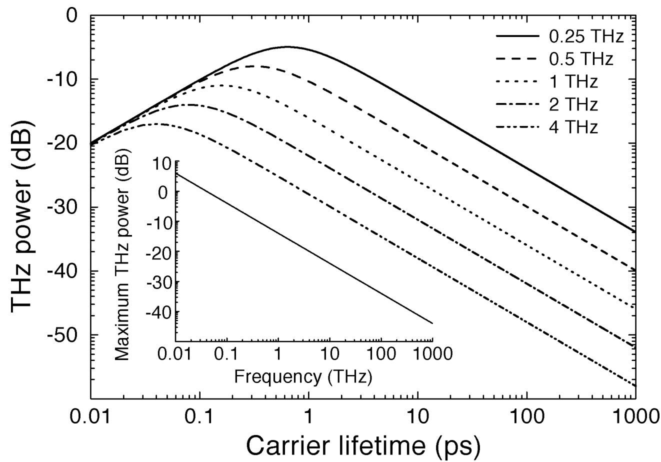

Fig. 4. Plots of the theoretical maximum terahertz power output as a function of the semiconductor trapping lifetime. As the frequency increases, the optimum lifetime decreases. Inset is the optimized power plotted as a function of frequency.

The lifetime dependence of the emitted terahertz power is plotted in Fig. 4 for a variety of beat frequencies. At any particular beat frequency, there exists a maxima as given by (11). If the carrier lifetime is too short, the carrier density never becomes large enough to produce a significant modulation in the conductivity. However, if the carrier lifetime becomes much longer than the beat period, then the accumulation of charge increases the heating in the device, which requires the bias to be decreased in order to avoid damage. Together with the screening effect of trapped carriers, this dramatically reduces the induced terahertz current, and hence the power available. Note that even under optimum conditions for each frequency, the maximum available terahertz power decreases by 3 dB per octave (see inset to Fig. 4). This is intrinsically a result of the generation process, which gives proportionally more energy dissipated as heat at higher frequencies.

To summarize, (10) predicts the conditions required to enable the power at any given frequency to be maximized. The performance of photomixing devices as a function of frequency is dictated by three effects. First, the finite time required for excited carriers to recombine τ greatly limits the performance as the frequency is increased. Second, the finite capacitance of the photoconductive gap allows an accumulation of charge at the electrodes. Again, this has the effect of reducing any modulation with frequencies greater than the corresponding RC time constant. Finally, the efficiency with which terahertz power is coupled out of the photomixer and radiated into free space will, in general, be frequency dependent, given by $R_A(\omega)$.

It is convenient to view the components associated with these three criteria independently, such that a modular approach may be taken to optimization. First, the carrier lifetime is optimized by use of low-temperature-grown gallium arsenide (LT-GaAs) grown and annealed under controlled conditions (Section III). The second design element is the optimization of the electrode geometry to control the capacitance, while simultaneously utilizing near-anode enhancements (Section IV). Finally, the efficiency of free-space coupling is optimized as a function of the impedance match between the photomixer and antenna (Section V). The mean impedance of the photoconductive gap may be estimated using (4), and putting typical values of $\bar{n} = 10^{15}$ cm^{-3}, $r = 5$ μm, $\mu = 1000$ cm^{2}V^{-1}s^{-1}, $A = 64$ μm^2, and $d = 1$ μm predicts the impedance of the photoconductive gap to be large $(> 10$ k$\Omega)$. Hence, the impedance of the antenna must be maximized at the desired frequency: resonant structures will be shown to increase power output by up to an order of magnitude at the target frequency when compared to conventional broadband antennas [25].

III. Material and Device Fabrication

For CW mixing in the frequency range 0.2–2 THz, optimum photocarrier lifetimes range from 80 to 800 fs. GaAs grown by molecular-beam epitaxy (MBE) has electron–hole recombination lifetimes of typically 10 ps–1 ns. The effective conduction band lifetime can be significantly reduced, however, through the introduction of mid bandgap traps. These might be associated with the inclusion of point defects in the GaAs lattice, and created, for example, either by post-growth ion-implantation, or by LT-GaAs [8], [26]–[28], as used in this work. Such defects can arise from an excess of arsenic, and they provide a large capture cross section for the trapping of conduction band electrons, leading to trapping times as short as 90 fs [29]. Subsequently, the material may be annealed to increase the resistivity, albeit with a corresponding increase in lifetime [30]. This compromise between short carrier lifetimes and high resistivities depends critically upon the precise growth and anneal conditions.

In fact, it has recently been shown that the optimum anneal temperatures lie well below those commonly reported, with appreciable beneficial effects occurring for temperatures as low as 300 °C [31]. This enables the production of photoconductive devices with high resistivities, and essentially no compromise in the carrier lifetimes, and is illustrated in Fig. 5, where the carrier lifetime and resistance of LT-GaAs is plotted as a function of anneal temperature. The lifetime was measured using time-resolved photoreflectance [28], [32]–[34] using 90-fs pulses from a Ti:sapphire laser operating at 800 nm (inset). The accuracy of such measurements is dependent upon the wavelength and power of the exciting laser, as well as the correct interpretation of various artifacts that can arise. In addition, photoreflectance curves take no account of the possible effect of the electric field on the lifetime [35], [36]. However, the technique provides valuable and quantitative estimates for the lifetime, which are sufficient for comparative measurements. The resistivity was characterized through measurement of the resistance of a test device, with a 5-μm photoconductive gap, as pictured inset in Fig. 9.

The excess arsenic incorporation during low-temperature growth results primarily in the formation of antisite defects (arsenic atoms located at gallium sites) and gallium vacancies. Annealing then provides the thermal activation energy, which allows individual defects to migrate through the material to form metallic precipitates. At any given annealing temperature, these defect concentrations will approach an equilibrium value as the duration of the anneal increases, according to the vacancy assisted diffusion mechanism applied by Bliss *et al.* [37]. The position of this equilibrium is a sensitive function of the anneal temperature: for temperatures in excess of 550 °C

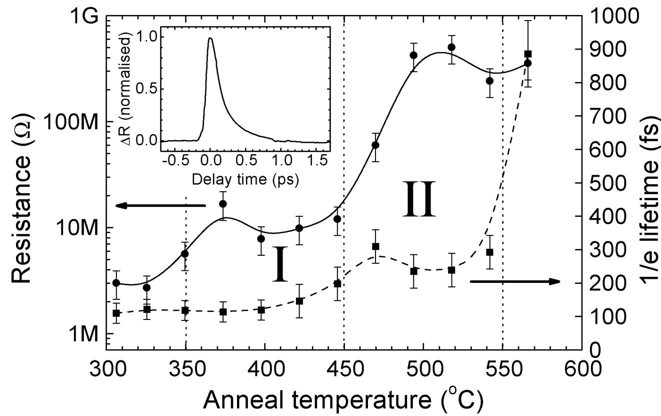

Fig. 5. The carrier lifetime and resistance of a photoconductive test device as a function of anneal temperature [31]. Material annealed in region I shows a substantial increase in resistance for no compromise in lifetime. In region II, the resistance increases by two orders of magnitude, for a small increase in the lifetime. Further increase of the temperature dramatically increases the lifetime, with little further increase in resistivity. Inset is a sample reflectivity curve for a 375 °C anneal.

though, there is essentially complete elimination of the point defects. Even at the lowest anneal temperatures, any change in the arsenic content is also accompanied by an increase in the resistivity of the material, and anneal temperatures between 350 °C and 550 °C (regions I and II in Fig. 5) were found to give the optimum combination of lifetime and resistance for CW photomixing.

For the photoconductive material in this work, LT-GaAs was deposited by MBE onto an undoped, semi-insulating (001) GaAs substrate. The wafers incorporated an epitaxial buffer layer of GaAs grown at 600°C followed by a 100-nm insulating AlAs to prevent parallel conduction through the substrate. This was followed by a 1-μm thick epilayer of GaAs grown at 200 °C±10 °C, with the temperature estimated using a thermocouple. Following growth, the wafers were annealed ex situ in a rapid thermal annealer under a nitrogen atmosphere, and with a semi-insulating GaAs wafer being used to passivate the surface and inhibit arsenic loss. The anneal was performed at a temperature of 475 °C for 10 min, producing a carrier lifetime of ~200 fs, and an estimated bulk resistivity of $\sim 10^5$ Ωcm.

The electrode structure and antenna fine-features were defined in polymethyl methacrylate (PMMA) resist using electron beam lithography, with lateral dimensions down to ~200 nm. The macroscopic antenna structure was then superimposed using optical lithography in a separate exposure. Both the photomixer electrodes and antennas consist of 20–20–400 nm of Ti–Pd–Au—the large thickness is necessary to aid heat conduction away from the photoconductor, and to allow large photocurrents (~1 mA) to flow without damage to the device.

IV. Photomixer Characterization

Previous studies of the optimum geometry for photomixers have investigated the distribution of the electric field in the gap, both laterally and as a function of depth [38]. It was found that the change in the trap occupation of the photoconductor close to metal-semiconductor junctions gives a highly nonuniform electric field distribution, leading to effects such as near-anode enhancement [21]. The electric field away from the electrodes is then much weaker, contributing little to the terahertz power. In fact, measurements have shown that almost 90% of the potential difference is dropped within a few microns of the anode [21]. For CW-THz photomixers, where the incident optical power is relatively low, it is advantageous to increase the active area for generation by adding interdigitated fingers to the electrodes. This effectively increases the length of the metal–semiconductor interface at the electrodes. It also increases the conductance and hence improves the impedance match with the antenna, but at the cost of increased device heating.

However, the inclusion of interdigitated photomixing elements also leads to an increased capacitance [16], which scales approximately with the active area in which photocarriers are excited. The area can be reduced to match the diffraction limited laser beam, but there are penalties in terms of the current limit for device damage, and resilience of the system to any drift in the laser beam alignment. Compromise is also necessary in the choice of dimensions for the interdigitated fingers and gaps. The metal fingers must be large enough to define using lithographic processes and sufficiently robust to withstand high photocurrents. However, if the width becomes too great, the photomixer becomes inefficient as much of the semiconductor is obscured. In the patterns assessed in this work, the active areas were varied from 4 μm × 4 μm up to 20 μm × 20 μm square, with the number of fingers in the pattern changed from 3 to 11, maintaining a finger separation of 1.7 μm.

To investigate the geometrical origin of the terahertz emission, a terahertz map of the photomixer was constructed by plotting the terahertz output as a function of the laser spot position on the active area. This experiment was performed using time-domain (pulsed) terahertz apparatus [12], with a femtosecond (120-fs pulse duration, 75-MHz repetition rate) laser being used to excite broadband terahertz pulses in the photomixer. Detection was fully optoelectronic, using a component separated from the original laser beam to gate the receiver. A rapid-scan delay line was used to collect the detected terahertz waveforms at a rate of 15 Hz. In each case, a standard 60 ° "bow-tie" antenna and 25-mm-diameter hyper-hemispherical silicon lenses were used to couple the radiation in and out of the semiconductors. Overviews of the emission and detection processes are given in [3].

To obtain the maps, the tightly focused laser spot (~ 1.7 μm) was raster scanned across the photomixer in both x and y directions. Thus carriers were created only in local areas of the finger pattern. The amplitude of the terahertz pulse is plotted as a function of position to produce an emission map of the photomixer. An example for the test device with a 5-μm gap is shown in Fig. 6, where the terahertz power is plotted for illumination along a straight line running from one electrode to the other, across the center of the gap, as illustrated inset. A diagram of the laser response function (assumed gaussian) is also included, and used to deconvolute the data, as shown by the dashed curve. The electrodes (shown shaded) cause no terahertz output when illuminated since no photoconduction is occurring. The near-anode enhancement is clear, with the terahertz power dropping by 58% within 1 μm of the electrodes. This effect is

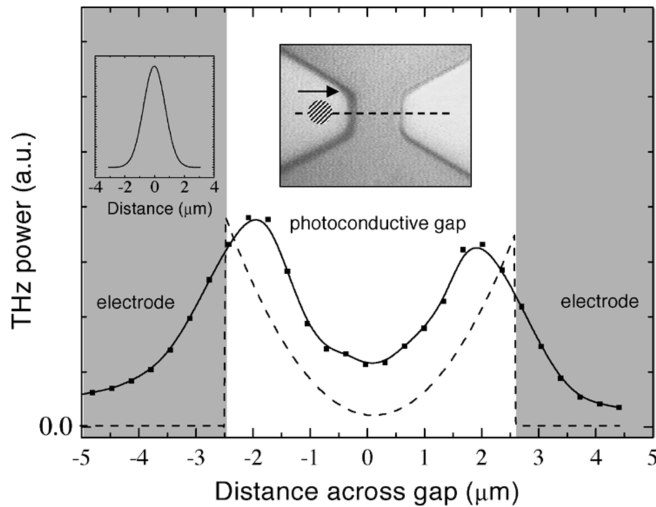

Fig. 6. Plot of terahertz-emitted power as a function of the laser excitation position in a 5-μm photoconductive gap (inset). The dashed curve shows the same data deconvoluted using the Gaussian laser response function (inset). The electric field profile may be deduced from this—over half of the potential difference occurs within 1 μm of the electrodes.

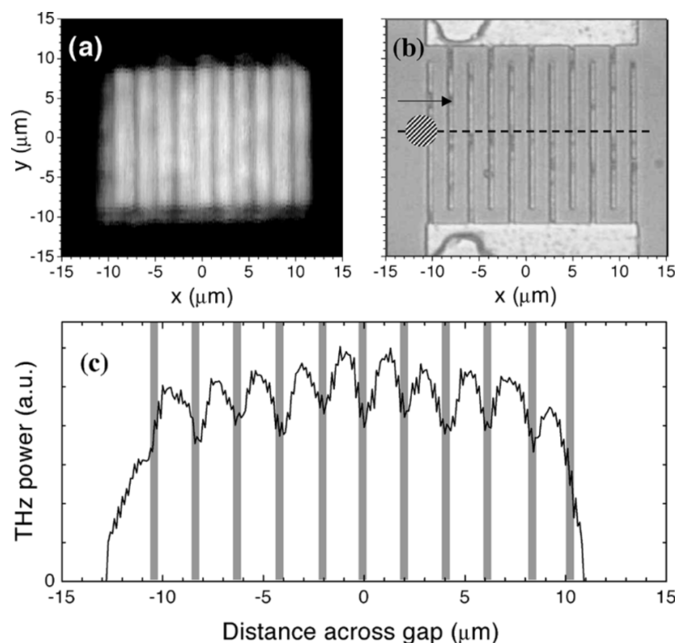

Fig. 7. (a) Image to show a 2-D terahertz map of the output power as a function of the position of the exciting laser spot. The areas for which the incident laser spot produces the least terahertz amplitude are shown in black, ranging to the largest detected amplitude shown in white. (b) Photograph of the structure, for comparison. Each image corresponds to a 30-μm square region of the photomixer. (c) Line-scan across the center of the device to show the convoluted terahertz power (and thus electric field profile) for a single y value, as shown dashed in the micrograph.

seen near to both electrodes, since the bias was alternated to facilitate lock-in detection.

Thus the design principle for the optimization of the finger separation in an interdigitated device is to maximize the field in the photoconductive gap by allowing the two enhanced regions to overlap. Fig. 7(a) shows the two-dimensional (2-D) terahertz map generated by a finger pattern with an active area of 20 μm $\times$ 20 μm and with 11 interdigitated fingers each of width 300 nm, a micrograph showing the same area of the emitter is also included [Fig. 7(b)].

Fig. 7(c) shows the raw (convoluted) data for the terahertz power profile extracted along a line of constant y, shown in the micrograph. Deconvoluting the response curve of the laser beam (not shown) yields an electric field profile with no sharp features, indicating that the field (and terahertz emission) is fairly constant across the device. Thus the minima in the raw data reflect only the loss of optical power owing to the laser beam being obscured by the electrodes. An optimum occurs when the lateral distance over which the electric field contributes to the terahertz power is comparable to both the finger spacing and the laser spot diameter (1–2 μm). Perhaps surprisingly, there is no significant enhancement in output at the fingertips, where electric field singularities might be assumed to increase the power substantially. All of these observations are in agreement with Cai *et al.* [22], who stated that the near-anode enhancement is absent in the small gap limit, without detailed explanation.

A pulsed terahertz system was used here as an assessment tool, because of its high signal-to-noise ratio (SNR) and ability to provide information for all frequencies. Although it is accepted that the generation mechanism of pulsed and CW-THz emission are subtly different, it is expected that a strong correlation will exist, since both will depend critically on the electric field profiles in and around the interdigitated finger patterns.

The photomixer designs assessed were next tested as CW-THz emitters, with excitation produced by two, independent, external-cavity diode lasers (TOPTICA Photonics DL100) operating at wavelengths around 850 nm, with a nominal instantaneous linewidth of order 1 MHz. The wavelength of each laser can be tuned by several nm, giving a beat frequency range of approximately 10 GHz–3 THz, with a $\sim$4 GHz mode spacing (resolution). The beams were made collinear using a 50:50 beamsplitter, giving a 40-mW combined beam, which was focused onto the photomixer elements using a 10$\times$ microscope objective. The terahertz radiation was coupled out of the rear surface of the substrate using a high-resistivity silicon lens, and detected with a silicon composite bolometer. The applied dc bias of up to 30 V was modulated at 200 Hz for lock-in detection. To prevent damage to the structure from Joule heating, the bias was limited by a dc current compliance of 0.75 mA. This corresponds to a total dissipated electrical power of approximately 25 mW—comparable to the incident optical power.

The emission power is plotted in Fig. 8 as a function of the laser difference frequency for photomixers with different numbers of fingers, but with a constant separation of the optimum 1.7 μm as characterized previously (micrographs shown inset, to scale). In each case, the photomixer is loading a broadband spiral antenna, consisting of self-complementary 4-turn spirals, with inner and outer final radii of 1.9 and 2.3 mm, respectively (shown inset to Fig. 10). The broad water vapor absorption band above 1 THz is clear in all cases, with the well-known spectral lines at 1.10, 1.16, and 1.41 THz also in evidence, as indicated by the arrows.

The performance of each design is broadly equivalent in the frequency range of 0.1–0.4 THz. Beyond this, the capacitive roll-off in output occurs at a higher frequency as the number

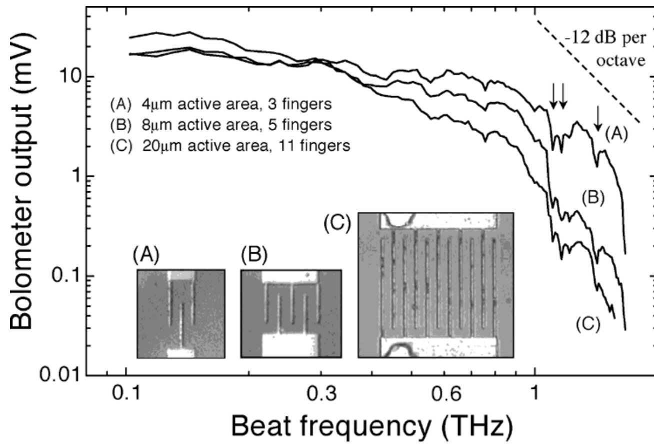

Fig. 8. Plot of the emitted power as a function of frequency for three of the devices tested. The inset micrographs (all at the same scale) show the geometry of the interdigitated-finger photomixers. At higher frequency, the power is seen to roll off more rapidly as the device capacitance increases. The dashed line shows the slope corresponding to a rolloff of -12 dB per octave, as predicted theoretically.

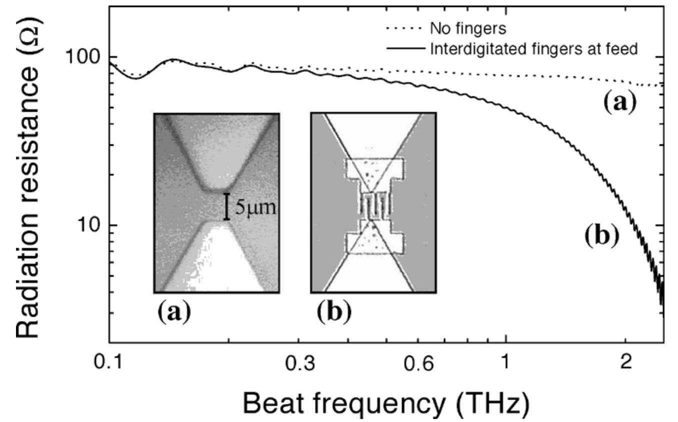

Fig. 9. Simulations of two bow-tie antennas with 5-μm photoconductive gaps (micrographs of the actual structures shown inset). (a) With a bare photoconductive gap. (b) With interdigitated fingers. For both structures, the antenna radiation impedance is plotted as a function of frequency. The capacitive effect of the fingers causes the effective impedance (and hence radiated power) to fall sharply as the frequency is increased. The fingers were modeled as a lumped capacitance of 1 fF; the oscillations at low and high frequencies are numerical artifacts.

of fingers and the active area is reduced. The decrease at high frequency (>1 THz) is characterized by -12 dB per octave, derived in (10). This difference amounts to more than an order of magnitude at 1.4 THz for devices A and C. Using an electromagnetic simulator in the frequency range 0–3 THz, numerical calculations predict the total capacitances to be approximately 2.8 and 18 fF, respectively. These are consistently greater than the values analytically calculated for similar structures by Brown *et al.* [39], owing to the inclusion of screening and the increased metallization thickness in our case. A photomixer capacitance of 2.8 fF, together with a 72-Ω spiral antenna, yields an RC time constant of 200 fs—a value comparable to the optimized photocarrier lifetime in LT-GaAs.

To summarize, the optimum finger spacing appears to lie close to the dimensions chosen by Brown *et al.* [38] (0.2-μm fingers separated by 1.8-μm gaps), and is independent of frequency. The optimum choice of total active area, in contrast, very much depends upon the working frequency of the photomixer. Equation (10) implies that the width of the photoconductive gap should be minimized to optimize the emitted power. However, this relationship holds only as long as the active area can be matched to the laser spot size, and is able to dissipate heat from the optical power. At higher frequencies, the need for a low capacitance dominates, to ensure that $\omega R_A C \ll 1$, requiring small active areas. At lower frequencies, however, the capacitance of the device is largely irrelevant. In fact, it may be preferable in this instance to use a larger active area. This would permit higher current flows within the device [and increased P_{Joule} from (10)], boosting the power from device C in Fig. 8, for which constant currents were employed. Furthermore, a larger device area will be less sensitive to beam drift from the CW lasers.

V. Antenna Characterization

The antenna transforms the terahertz current in the photomixer into an electromagnetic wave that can propagate in free space. The characteristic impedance of free space is $120\pi\Omega$, independent of frequency. However, the real part of the photomixer output impedance as seen by the antenna is frequency dependent and much higher (of order 10 kΩ) [25]. Thus in practice, impedance matching is difficult, and the radiated power scales with the input impedance presented by the antenna. For pulsed terahertz systems, a broad range of frequencies (typically between 50 GHz and 2 THz) are simultaneously generated. In this case, the antenna must be efficient over a wide frequency range, leading to the widespread use of bow-tie antenna designs. These are intrinsically broadband and easy to fabricate. An alternative type of broadband antenna design is the self-complementary log-spiral with a central feed [18]. The radiation impedance of this design is largely frequency independent, with a nominal calculated value of 72 Ω (for any self-complementary geometry), in a GaAs dielectric half space [16].

For our antenna designs, we calculated numerically the antenna input impedance as a function of frequency, using commercially available electromagnetic simulation software [40]. The substrate–air interface and antenna geometry were defined within a finite-element mesh and metal electrodes added as perfect electrical conductors. The photomixer was modeled by generating a gaussian wave packet in the gap and examining the frequency-dependent complex current and voltage at the antenna feed. The effect of including interdigitated fingers at the feed-point was modeled by a lumped capacitance in parallel with the photoconductive active area. The capacitance was calculated numerically for each geometry using the same software.

The calculated response is shown in Fig. 9, for a truncated 60° bow-tie antenna with a 5-μm photoconductive gap [inset (a) to Fig. 9]. It may be immediately seen that the bare antenna does have a relatively flat response (dotted line), dropping from 90 Ω at low frequencies to about 70 Ω at 2 THz, as expected. When an interdigitated photomixer feed [inset (b) to Fig. 9], is added to the antenna, the additional capacitance causes the net impedance presented to the photomixer to fall dramatically at

frequencies beyond 1 THz. The decrease in power is an order of magnitude at 2 THz.

For coupling of terahertz standing wave oscillations from the antenna, it is necessary for the antenna to have features on the effective length scale of the emitted terahertz wavelengths. Thus broadband antennas are designed with a fractal geometry: both the bow-tie and the spiral antenna designs fall into this category. However, for CW-THz systems, intended for operation at a single frequency, it is often desirable to maximize the input impedance at a single, target frequency. Modeling and experimental work has begun to address the use of resonant dipole antennas for this purpose [41]. However, only recently have such antennas been optimized to enhance the monochromatic emission from photomixers [25]. Duffy *et al.* used this concept to obtain higher frequency operation (beyond 2 THz). This was achieved by using the inductance present in dual dipole antennas to tune out the capacitance, thus increasing the frequency threshold for capacitive roll-off. Resonances at frequencies up to 2.7 THz were achieved, with the peak power subject only to the -6 dB per octave roll-off owing to the carrier lifetime. For our work, in contrast, we sought to design low-frequency (<1 THz) resonant antennas that increase power output in emission, and SNR in detection.

The resonant behavior of a center-feed dipole antenna (300 μm long, 8 μm wide, and of 1 μm thickness) was modeled numerically, and predicted a clear impedance resonance, shown in Fig. 10. The magnitude of the resonant power output was increased substantially by the use of quarter-wave choke elements to prevent radiative power loss along the bias transmission lines. Although previous work also included the effect of ohmic losses in the conductors [25], in our case there is no significant effect on the value of the resonant frequency, or the optimization condition. A decrease in the power output and Q-factor would be expected: but the effect is less severe because the dimensions of the conductors are increased (10–20 μm in width and 440 nm in thickness) relative to the 1 μm conductors in [25].

This antenna was then fabricated, with the dipole antenna, photomixer and choked feeds being defined lithographically on annealed LT-GaAs with a sub-200-fs lifetime. Using a CW-THz system, the emitted power was then measured as a function of the beat frequency, using a silicon composite bolometer, and Fig. 10 shows the predicted bolometer signal plotted as a function of frequency for the choked dipole antenna, together with experimental data for both (a) choked dipole and (b) spiral antennas.

The simulation predicted a resonance at 0.41 THz with a peak drive-point impedance of 270 Ω, and a full-width at half-maximum (FWHM) of 40 GHz. Experimentally, excellent agreement was seen, with a resonance occurring at 0.40 THz with a FWHM of 80 GHz. The resonance increases the power output by over 6.5 dB, compared to that achieved with the broadband spiral antenna fabricated on the same material, and excited in an identical way. The width of the resonance appears greater than predicted by the model, and may be associated with ohmic losses in the metallic structures. However, the experimental resonance is still much narrower than seen previously for this type of antenna: the responses reported in [2], [25]

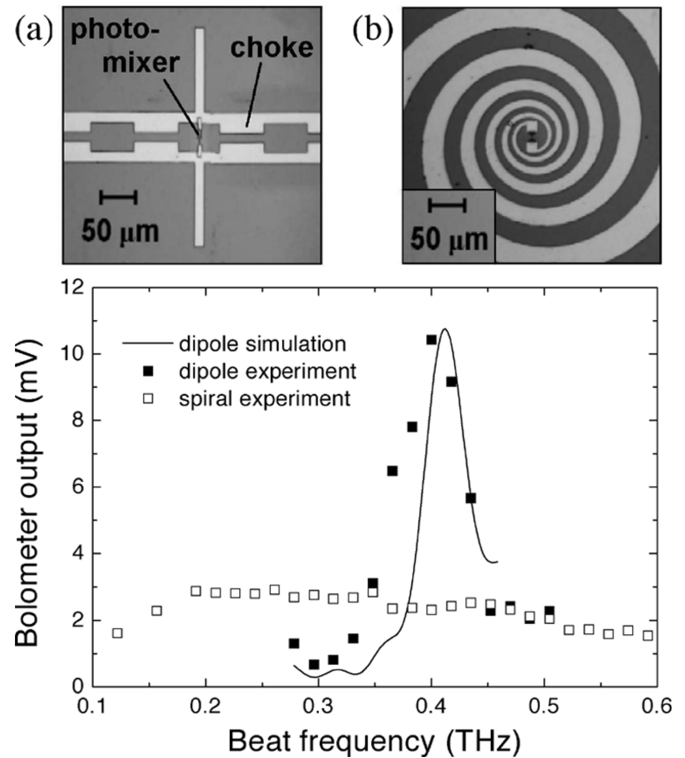

Fig. 10. Simulated and experimental results from (a) 300-μm dipole and (b) broadband spiral. The simulation data (curve) has been normalized with respect to the experimental results at resonance.

typically exceeded 200 GHz in width, at central frequencies of 0.7–1.0 THz. The reason for this difference is not clear at present.

The resonant antenna was then used as a receiver, in place of the bolometer, and gated using the beat frequency of the lasers, with a total incident power of 20 mW. The relative phase between the incident terahertz radiation and the beat envelope was changed using a delay line, generating an interferogram. The Fourier transform is then the convoluted frequency response of both emitter and detector. Initially, a resonant antenna and broadband (spiral) receiver were characterized for reference. When a resonant receiver matched to the emitter was substituted, the detected signal amplitude increased by 9.8 dB at 0.4 THz. An added benefit of this approach is that the detector now also acts as a filter, and thus any RF components are largely rejected.

VI. Polarization Measurements

The polarization of the emitted terahertz radiation can be related to the geometry of the antenna. A bolometer is essentially insensitive to both frequency and polarization, and so to measure the polarization experimentally, a wire-grid terahertz polarizer was inserted into the terahertz path. Detected powers were measured as a function of both frequency and polarizer angle for spiral, bow-tie and dipole antennas, across the entire measurable frequency range with the angle between the polarizing filter elements and the long axis of the interdigitated fingers varied between 0 and 180°. The ratio between the minimum and maximum powers transmitted through the polarizer may be

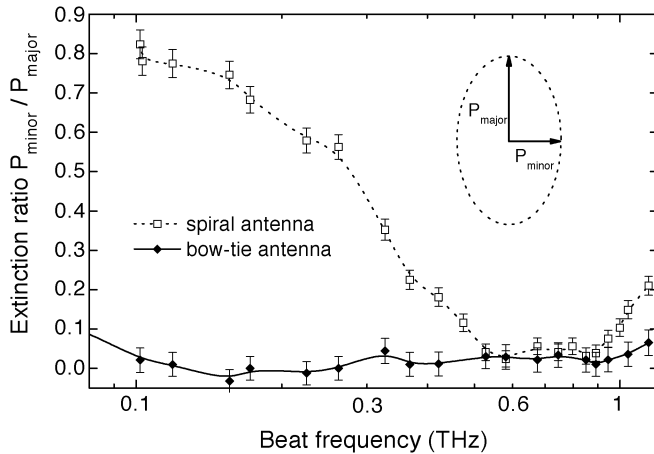

Fig. 11. Extinction ratio (minor/major) of the elliptically polarized emitted terahertz as a function of frequency. A value of 0 corresponds to a perfectly linear polarization, whereas a value of 1 indicates a perfectly circular polarization state.

used to define the extinction ratio. This is plotted in Fig. 11 for an 8 μm $\times$ 8 μm photomixer coupled to both a broadband spiral (dotted line) and simple bow tie antenna (solid line).

Fig. 11 shows that the bow-tie antenna emission is linearly polarized over the entire frequency range, with an extinction ratio of order 1:20. A similar experiment was performed for a resonant dipole antenna, and the linear polarization state at resonance had an extinction ratio of better than 1:650. This is expected because the electric field is directed along the dipole length. The emission from the spiral, however, is almost circularly polarized (orthogonal components equal) at 0.1 THz, but this state becomes increasingly elliptically polarized as the frequency rises. Above 0.6 THz, the emission is essentially linear, as for the bow tie antenna. The change in the polarization state with frequency in the spiral antenna may be attributed to the change in the antenna geometry as seen by different wavelengths. Wavelengths that are resonant with the spiral arms will be emitted with a circular polarization.

To illustrate this further, Fig. 12 shows the terahertz power on a polar plot, as a function of the angle between the interdigitated fingers and the transmission axis of the wire grid polarizer. It may be seen that as the emitted terahertz radiation becomes more elliptically polarized with increasing frequency, the orientation of the major axis of polarization also rotates, following the direction of the spiral antenna arms. As the linear limit is approached at the center of the spiral, this major axis becomes oriented parallel to the interdigitated fingers on the photomixer. Thus we deduce that in this regime, the emission is radiated directly from linear dipole resonances in the interdigitated fingers. The linearly polarized output from the bow-tie (and dipole) antennas is always in the direction parallel to the fingers over the measurable frequency range.

Polarization measurements were then repeated with similar antenna structures, using a pulsed terahertz system based on the femtosecond laser. The improved SNR allowed an assessment at much higher frequency, and with the advantage that the polarization may be measured for all frequencies simultaneously. A pair of time domain traces with the terahertz grid polarizer

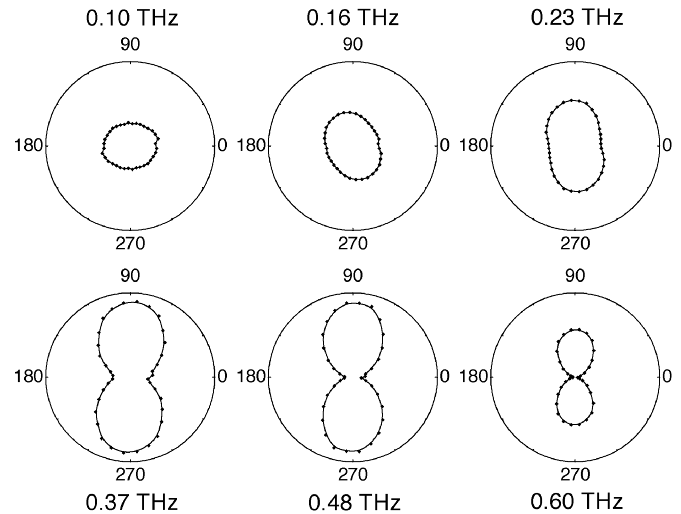

Fig. 12. Polar plots of the terahertz radiation emitted from the spiral antenna at frequencies of 0.10, 0.16, 0.23, 0.37, 0.48, and 0.60 THz. 0° and 90° correspond to the components of terahertz power with the electric field perpendicular and parallel to the fingers, respectively.

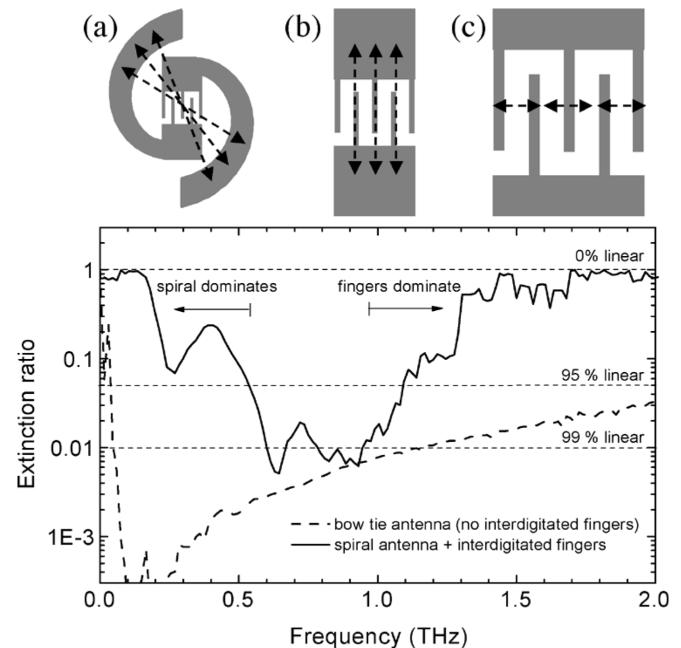

Fig. 13. Extinction ratio, derived from the Fourier transforms of orthogonal components, plotted as a function of frequency. The bow tie antenna without interdigitated fingers (dotted line) has a linear polarization across the whole frequency range. The spiral antenna with fingers (solid line) has a more complicated dependence, owing to the spiral structure at low frequency (below 0.6 THz) and to the fingers at high frequency (above 1.1 THz). Thus the dependence may be divided into three regimes, where the effective wavelength is on the scale of (a) the spiral arms, (b) the finger length, and (c) the finger separation.

in orthogonal orientations were obtained. By dividing the corresponding Fourier transforms, the extinction ratio as a function of frequency was deduced. Fig. 13 shows the frequency dependence of the extinction ratio, defined once again, as the ratio of the power emitted with the terahertz electric field perpendicular to the fingers, to the power emitted with the electric field orientated parallel to the fingers. Thus a value of 0 corresponds to the terahertz linear polarization being entirely parallel to the fingers,

while a value of 1 describes a situation where the components in the orthogonal directions are equal.

The dashed line in Fig. 13 shows results for a bow-tie antenna with no photomixer fingers. As with the CW measurements, a linear polarization (more than 95% linear) is observed across the entire frequency range, with the major axis aligned parallel to the bias field in the photoconductive gap. The solid line shows the analogous curve for a spiral antenna with interdigitated fingers defined at the center, shown inset on various scales. A value of unity is measured for the extinction ratio at low frequency, indicating circular polarization below 0.2 THz, where the effective wavelength is on the scale of the spiral arms [inset (a)]. As with the CW measurements, the polarization is elliptical between 0.2 and 0.6 THz. The peak at 0.4 THz is reproducible, and may be due to a resonance at the finger-spiral interface. This may be an artifact of the processing technique, since the fingers and spiral were necessarily defined in two separate metallization processes. Between 0.6 and 1.1 THz, the polarization is linear, and aligned parallel with the fingers. Again, this is in agreement with the CW measurements, and suggests that the emission in this frequency range arises from a resonance on the length scale of the fingers [inset (b)]. At frequencies above 1.3 THz, corresponding to length scales substantially below the resonance lengths of the fingers, a component in the perpendicular direction (i.e., directly radiated from current transients in the semiconductor material between the fingers) becomes observable [Fig. 13(c)]. This causes the extinction ratio to rise rapidly with increasing frequency for the emitter with fingers. The similarity of the polarization behavior with increasing frequency for both pulsed and CW-THz sources justifies the assertion that the role of the antenna is identical in each case, and distinct from the photomixer, where differences may occur owing to the vast different in peak carrier densities between the two cases.

The idea of a characteristic length scale is central to the theory of dipole antennas in radio or microwave applications. The analogous theory for planar terahertz transceivers takes into account a modification owing to the dielectric half-space of GaAs ($\epsilon = 12.8$). For the fundamental (half-wave) dipole resonance, the effective resonant length scale d_{eff} is given by [42]

$$d_{\mathrm{eff}} \sim \frac{\lambda_{\mathrm{free}}}{2\sqrt{\frac{(\epsilon+1)}{2}}} \sim \frac{\lambda_{\mathrm{free}}}{5.25}. \tag{12}$$

However, experiments using full- and half-wave dipoles [41] show that these simple arguments are incomplete, whereas our polarization measurements yield direct estimations of these length scales. The polarization state of the emission from the spiral antenna changes from elliptical to linear at a frequency of approximately 0.6 THz, where the calculated half-wavelengths in free space and the GaAs half-space are 250 and 95 μm, respectively. In contrast, the corresponding physical length scale at the spiral center where this polarization change occurs is only 20–60 μm; such discrepancies occur since (12) holds only for an ideal isolated, thin dipole. In fact, the resonant behavior of real devices is strongly perturbed by both the finite structure width and thickness, as well as the electrical response of the adjoining bond wires—a conclusion supported by our numerical modeling.

VII. Conclusion

We have outlined a systematic approach for the improvement of CW emitters and receivers that operate on the principle of photomixing. The photoconductor, electrode geometry and antenna have each been independently optimized according to the individual criteria from our theoretical model.

There are advantages in using CW-THz radiation for commercial imaging and spectroscopy systems, compared to the more established pulsed technologies. The narrow bandwidth yields a very high spectral density, allowing improved frequency resolution and faster scanning times [24]. Furthermore, use of inexpensive diode lasers in a portable terahertz system will be compact, robust, genuinely turn-key and of low cost [19]. However, diode lasers provide relatively little power, and thus increasing the efficiency of both the photomixers and antennas are key steps toward achieving their practical implementation.

References

[1] D. H. Auston, "Picosecond optoelectronic switching and gating in silicon," *Appl. Phys. Lett.*, vol. 26, no. 3, pp. 101–103, 1975.

[2] P. R. Smith, D. H. Auston, and M. C. Nuss, "Subpicosecond photoconducting dipole antennas," *IEEE J. Quantum Electron.*, vol. 24, no. 2, pp. 255–260, Feb. 1988.

[3] P. U. Jepsen, R. H. Jacobsen, and S. R. Keiding, "Generation and detection of terahertz pulses from biased semiconductor antennas," *J. Opt. Soc. Amer. B.*, vol. 13, no. 11, pp. 2424–2436, 1996.

[4] R. Köhler, A. Tredicucci, F. Beltram, H. E. Beere, E. H. Linfield, A. G. Davies, D. A. Richie, R. C. Iotti, and F. Rossi, "Terahertz semiconductor-heterostructure laser," *Nature*, vol. 417, pp. 156–159, 2002.

[5] M. C. Kemp, P. F. Taday, B. E. Cole, J. A. Cluff, A. J. Fitzgerald, and W. R. Tribe, "Security applications of terahertz technology," *Proc SPIE*, vol. 5070, pp. 44–52, 2003.

[6] D. D. Arnone, C. M. Ciesla, and M. Pepper, "Terahertz imaging comes into view," *Phys. World*, vol. 13, no. 4, pp. 35–40, 2000.

[7] J. V. Rudd and D. M. Mittleman, "Influence of substrate-lens design in terahertz time-domain spectroscopy," *J. Opt. Soc. Amer. B*, vol. 19, no. 2, pp. 319–329, 2002.

[8] F. W. Smith, H. Q. Le, V. Diadiuk, M. A. Hollis, A. R. Calawa, S. Gupta, M. Frankel, D. R. Dykaar, G. A. Mourou, and T. Y. Hsiang, "Picosec-ond GaAs-based photoconductive optoelectronic detectors," *Appl. Phys. Lett.*, vol. 54, no. 10, pp. 890–892, 1989.

[9] Y. Chen, S. Williamson, T. Brock, F. W. Smith, and A. R. Calawa, "375-GHz-bandwidth photoconductive detector," *Appl. Phys. Lett.*, vol. 59, no. 16, pp. 1984–1986, 1991.

[10] M. Tani, K. Sakai, and H. Mimura, "Ultrafast photoconductive detectors based on semi-insulating GaAs and InP," *Jpn. J. Appl. Phys.*, vol. 36, no. 2, pp. L1175–L1178, 1997.

[11] S. Kono, M. Tani, P. Gu, and K. Sakai, "Detection of up to 20 THz with a low-temperature-grown GaAs photoconductive antenna gated with 15 fs light pulses," *Appl. Phys. Lett.*, vol. 77, no. 25, pp. 4104–4106, 2000.

[12] C. Baker, I. S. Gregory, W. R. Tribe, I. V. Bradley, M. J. Evans, M. Withers, P. F. Taday, V. P. Wallace, E. H. Linfield, A. G. Davies, and M. Missous, "Terahertz pulsed imaging with 1.06 μm laser excitation," *Appl. Phys. Lett.*, vol. 83, no. 20, pp. 4113–4115, 2003.

[13] B. B. Hu and M. C. Nuss, "Imaging with terahertz waves," *Opt. Lett.*, vol. 20, no. 16, pp. 1716–1718, 1995.

[14] D. M. Mittleman, R. H. Jacobsen, and M. C. Nuss, "T-ray imaging," *IEEE J. Sel. Topics Quantum Electron.*, vol. 2, no. 3, pp. 679–692, May–Jun. 1996.

[15] E. R. Brown, F. W. Smith, and K. A. McIntosh, "Coherent millimeter-wave generation by heterodyne conversion in low-temperature-grown GaAs photoconductors," *J. Appl. Phys.*, vol. 73, no. 3, pp. 1480–1484, 1993.

[16] E. R. Brown, K. A. McIntosh, K. B. Nichols, and C. L. Dennis, "Photomixing up to 3.8 THz in low-temperature-grown GaAs," *Appl. Phys. Lett.*, vol. 66, no. 3, pp. 285–287, 1995.

[17] S. Verghese, K. A. McIntosh, S. Calawa, W. F. Dinatale, E. K. Duerr, and K. A. Molvar, "Generation and detection of coherent terahertz waves using two photomixers," *Appl. Phys. Lett.*, vol. 73, no. 26, pp. 3824–3826, 1998.

[18] S. Verghese, K. A. McIntosh, and E. R. Brown, “Highly-tunable fiber-coupled photomixers with coherent terahertz output power,” *IEEE Trans. Microw. Theory Tech.*, vol. 45, no. 8, pp. 1301–1309, Aug. 1997.
[19] I. S. Gregory, W. R. Tribe, B. E. Cole, C. Baker, M. J. Evans, I. V. Bradley, E. H. Linfield, A. G. Davies, and M. Missous, “Phase sensitive continuous-wave THz imaging using diode lasers,” *Electron. Lett.*, vol. 40, no. 2, pp. 143–145, 2004.
[20] M. B. Johnston, D. M. Whittaker, A. Corchia, A. G. Davies, and E. H. Linfield, “Simulation of terahertz generation at semiconductor surfaces,” *Phys. Rev. B*, vol. 65, pp. 1653011–1653018, 2002.
[21] S. E. Ralph and D. Grischkowsky, “Trap-enhanced electric fields in semi-insulators: the role of electrical and optical carrier injection,” *Appl. Phys. Lett.*, vol. 59, no. 16, pp. 1972–1974, 1991.
[22] Y. Cai, I. Brener, J. Lopata, J. Wynn, L. Pfeiffer, and J. Federici, “Design and performance of singular electric field terahertz photoconducting antennas,” *Appl. Phys. Lett.*, vol. 71, no. 15, pp. 2076–2078, 1997.
[23] T. Kleine-Ostmann, P. Knobloch, M. Koch, S. Hoffman, M. Breede, M. Hofmann, G. Hein, K. Pierz, M. Sperling, and K. Donhuijsen, “Continuous-wave THz imaging,” *Electron. Lett.*, vol. 37, no. 24, pp. 1461–1462, 2001.
[24] K. J. Siebert, T. Löffler, H. Quast, M. Thomson, T. Bauer, R. Leonhardt, C. Czasch, and H. G. Roskos, “All-optoelectronic continuous wave THz imaging for biomedical applications,” *Phys. Med. Biol.*, vol. 47, pp. 3743–3748, 2002.
[25] S. M. Duffy, S. Verghese, K. A. McIntosh, A. Jackson, A. C. Gossard, and S. Matsuura, “Accurate modeling of dual dipole and slot elements used with photomixers for coherent terahertz output power,” *IEEE Trans. Microw. Theory Tech.*, vol. 49, no. 6, pp. 1032–1038, Jun. 2001.
[26] S. Gupta, M. Y. Frankel, J. A. Valdmanis, J. F. Whitaker, G. A. Mourou, F. W. Smith, and A. R. Calawa, “Subpicosecond carrier lifetime in GaAs grown by molecular beam epitaxy at low temperatures,” *Appl. Phys. Lett.*, vol. 59, no. 25, pp. 3276–3278, 1991.
[27] S. Gupta, J. F. Whitaker, and G. A. Mourou, “Ultrafast carrier dynamics in III-V semiconductors grown by molecular-beam epitaxy at very low substrate temperatures,” *IEEE J. Quantum Electron.*, vol. 28, no. 10, pp. 2464–2472, Oct. 1992.
[28] H. S. Loka, S. D. Benjamin, and P. W. E. Smith, “Optical characterization of low-temperature-grown GaAs for ultrafast all-optical switching devices,” *IEEE J. Quantum Electron.*, vol. 34, no. 8, pp. 1426–1437, Aug. 1998.
[29] K. A. McIntosh, K. B. Nichols, S. Verghese, and E. R. Brown, “Investigation of ultrashort photocarrier relaxation times in low-temperature-grown GaAs,” *Appl. Phys. Lett.*, vol. 70, no. 3, pp. 354–356, 1997.
[30] J. K. Luo, H. Thomas, D. V. Morgan, and D. Westwood, “Transport properties of GaAs layers grown by molecular beam epitaxy at low temperature and the effects of annealing,” *J. Appl. Phys.*, vol. 79, no. 7, pp. 3622–3629, 1996.
[31] I. S. Gregory, C. Baker, W. R. Tribe, M. J. Evans, H. E. Beere, E. H. Linfield, A. G. Davies, and M. Missous, “High resistivity annealed low-temperature GaAs with 100 fs lifetimes,” *Appl. Phys. Lett.*, vol. 83, no. 20, pp. 4199–4201, 2003.
[32] S. Sinha, B. M. Arora, and S. Subramanian, “Photoreflectance and photoluminescence spectroscopy of low-temperature GaAs grown by molecular-beam epitaxy,” *J. Appl. Phys.*, vol. 79, no. 1, pp. 427–432, 1996.
[33] J.-S. Yu, H.-C. Ho, S. Horng, and C.-C. Chi, “Spectral dependence of time-resolved photoreflectance of low-temperature-grown GaAs,” *Jpn. J. Appl. Phys.*, vol. 36, no. 4A, pp. 2144–2150, 1997.
[34] M. Stellmacher, J. Nagle, J. F. Lampin, P. Santoro, J. Vaneecloo, and A. Alexandrou, “Dependence of the carrier lifetime on acceptor concentration in GaAs grown at low-temperature under different growth and annealing conditions,” *J. Appl. Phys.*, vol. 88, no. 10, pp. 6026–6031, 2000.
[35] N. Zamdmer, Q. Hu, K. A. McIntosh, and S. Verghese, “Increase in response time of low-temperature-grown GaAs photoconductive switches at high voltage bias,” *Appl. Phys. Lett.*, vol. 75, no. 15, pp. 2313–2315, 1999.
[36] K.-G. Gan, J.-W. Shi, Y.-H. Chen, C.-K. Sun, Y.-J. Chiu, and J. E. Bowers, “Ultrahigh power-bandwidth-product performance of low-temperature-grown-GaAs based metal-semiconductor-metal traveling wave photodetectors,” *Appl. Phys. Lett.*, vol. 80, no. 21, pp. 4054–4056, 2002.
[37] D. E. Bliss, W. Walukiewicz, and E. E. Haller, “Annealing of As_{Ga} -related defects in LT-GaAs: the role of gallium vacancies,” *J. Electron. Mater.*, vol. 22, no. 12, pp. 1401–1404, 1993.
[38] E. R. Brown, “A photoconductive model for superior GaAs THz photomixers,” *Appl. Phys. Lett.*, vol. 75, no. 6, pp. 769–771, 1999.
[39] K. A. McIntosh, E. R. Brown, K. B. Nichols, and O. B. McMahon, “Terahertz photomixing with diode lasers in low temperature-grown GaAs,” *Appl. Phys. Lett.*, vol. 67, no. 26, pp. 3844–3846, 1995.
[40] Computer simulation technology. [Online]. Available: http://www.cst.de
[41] K. A. McIntosh, E. R. Brown, K. B. Nichols, O. B. McMahon, W. F. DiNatale, and T. M. Lyszczarz, “Terahertz measurements of resonant planar antennas coupled to low-temperature-grown GaAs photomixers,” *Appl. Phys. Lett.*, vol. 69, no. 24, pp. 3632–3634, 1996.
[42] M. Tani, M. Watanabe, and K. Sakai, “Photoconductive twin dipole antennas for THz transceiver,” *Electron. Lett.*, vol. 38, no. 1, pp. 5–6, 2002.

Ian S. Gregory was born in Stoke-on-Trent, U.K., in 1979. He received the M.Phys. (hons) degree in physics from the University of Sheffield, Sheffield, U.K., in 2001, and is currently pursuing the Ph.D. degree at the Semiconductor Physics Group, University of Cambridge, Cambridge, U.K.

He holds a CASE award with TeraView Ltd., Cambridge, U.K., and has now joined their expanding Research and Development Group, working on the development of continuous-wave terahertz sources and detectors based on photomixing using diode lasers.

Colin Baker was born in Ormskirk, U.K., in 1977. He received the B.Sc. degree in physics from the University of Sheffield, Sheffield, U.K. in 2000, and the Ph.D. degree in physics from the University of Cambridge, Cambridge, U.K., in 2004.

He is currently employed as a member of the security group at TeraView Ltd, Cambridge, U.K., and his research interests include the application of high-power coherent terahertz photoconductive devices for security screening, and the development of cost effective, compact, and commercially viable terahertz systems.

William R. Tribe was born in London, U.K., in 1969. He received the B.Sc. (hons) degree in physics from Imperial College, London University, London, in 1990, and the D.Phil. in the optical properties of semiconductors from the Clarendon Laboratory, Oxford University, Oxford, U.K., in 1994.

Following academic posts at Sheffield University, Sheffield, U.K., (1994–1996), and the Cavendish Laboratory, Cambridge University, Cambridge, U.K., (1996–2001), studying the electronic and optical properties of semiconductor materials and devices, he moved to TeraView Ltd., Cambridge. He now heads an research and development division responsible for developing novel terahertz systems and devices including pulsed and continuous-wave systems and is Technical Lead for applications development in the security area.

Ian V. Bradley was born in Omagh, Northern Ireland, U.K., in 1967. He received the B.Sc. (hons) degree in physics in 1988 and the M.Sc. degree in optoelectronics and optical signal processing from Queen University of Belfast, Belfast, U.K., in 1989. He received the Ph.D. degree in interdiffusion of III–V semiconductors heterostructures from Surrey University, Surrey, U.K.

Following academic posts at Strathclyde University in Glasgow, Glasgow, U.K., (1994–1997), University of Nagoya, Nagoya, Japan (1997–1999), and Felix Free Electron Facility, The Netherlands (1999–2001) studying the optical properties of semiconductor materials, he moved to TeraView Ltd., Cambridge, U.K., in 2001. He is currently part of the engineering group within the company.

Michael J. Evans was born in Gloucester, U.K., in 1964. He received the B.Sc. degree in materials science from the University of Surrey, Surrey, U.K., in 1988, and the M.Sc. degree in microelectronics from the University of Manchester Institute of Science and Technology (UMIST), Manchester, U.K., in 1990.

He is currently employed as a Device Engineer at Teraview Ltd., Cambridge, U.K., and is working on the development of terahertz sources and detectors.

Edmund H. Linfield received the B.A. degree in physics and the Ph.D. degree in semiconductor physics from the University of Cambridge, Cambridge, U.K., in 1986 and 1991, respectively.

He is currently Professor of Terahertz Electronics at the University of Leeds, Leeds, U.K. His research interests include the development and applications of terahertz systems, quantum cascade lasers, molecular beam epitaxial growth, and low-dimensional electronic systems.

A. Giles Davies received the B.Sc. degree in chemical physics from the University of Bristol, Bristol, U.K., in 1987, and the Ph.D. degree in semiconductor physics from the University of Cambridge, Cambridge, U.K., in 1991.

He is currently Professor of Electronic and Photonic Engineering at the University of Leeds, Leeds, U.K. His research interests concentrate on the electrical and optical properties of low-dimensional electronic systems, multilayered semiconductor devices, and nanotechnology, with particular recent focus on the development of terahertz frequency systems, and the exploitation of biological processes for nanoscale assembly.

Mohamed Missous (M'95) received the Ph.D. degree from University of Manchester Institute of Science and Technology (UMIST), Manchester, U.K., in 1985, focusing on the molecular beam epitaxial (MBE) growth of metals and semiconductors.

He became Chair of Semiconductor Materials and Devices, UMIST, in 2001. All his research has been closely associated with the MBE effort at the UMIST, and recently, has concentrated with considerable success on establishing practical approaches and techniques required to meet stringent doping and thickness, control for a variety of advanced quantum devices. This has included work on GaAs, AlGaAs, InGaAs, InAlAs, InGaP, and InAlP. His principal research interests are interfaces, both metal–semiconductor and semiconductor–semiconductor, and MBE growth mechanisms, especially under conditions of exact stoichiometry at low temperatures. He is actively involved as a Consultant to both the microwave industries in the U.K., Japan, and the U.S. He has published over 150 papers on MBE related topics.